Chemical Science

ROYAL SOCIETY OF CHEMISTRY

EDGE ARTICLE

View Article Online
View Journal | View Issue

Cite this: *Chem. Sci.*, 2025, **16**, 23262

All publication charges for this article have been paid for by the Royal Society of Chemistry

Single site of water-resistant asymmetric Bi–Ov–Mn for robust VOC ozonation at ambient temperature

Yuqin Lu, †[abcd] Huayang Zhang, †[df] Hua Deng, *[abc] Jianguo Ding,[abc] Tingting Pan,[abc] Wenjie Tian,[df] Yunbo Yu,[ce] Changbin Zhang,[ce] Wenpo Shan,[bc] Shaobin Wang,[d] Hong He *[bce] and Joseph S. Francisco *[g]

Received 13th August 2025
Accepted 24th October 2025

DOI: 10.1039/d5sc06166k

rsc.li/chemical-science

Manipulating the geometries and electronic structures of oxygen vacancies (Ovs) in oxides to increase their catalytic activity has been a critical focus of research, but the processes remain challenging, particularly because of the significant interference caused by ubiquitous water vapour. In this work, we employ a nanocrystal-to-crystal transformation methodology to integrate a single atom of bismuth (Bi) into MnO_2, resulting in the formation of Bi–Ov–Mn entities. This single site reduces the formation energy of $^{\bullet}OOOH$ species, facilitating the formation of reactive oxygen species (ROS), particularly $^{\bullet}OH$, due to the nonuniform electron distribution in the presence of both ozone and water. Therefore, this unique asymmetric defective linkage provides excellent water vapour resistance (1.8 vol%), which significantly improves its performance in the removal of volatile organic compounds. In this study, a pioneering paradigm utilizing asymmetric active sites is introduced, which expands the potential of catalytic ozonation for VOC abatement.

Introduction

Metal oxides, including MnO_2,[1,2] CeO_2,[3] ZnO,[4] TiO_2,[5] and Co_3O_4,[6] are becoming increasingly critical in catalytic chemistry for energy conversion and environmental protection practices. Oxygen vacancies (Ovs) are ubiquitous on these reducible oxides, providing a powerful force for driving surface chemistry and catalytic reactions.[7,8] For example, in the oxidation of organic compounds,[9] Ovs govern redox ability and ultimately determine catalytic activity and stability.

Since Ovs are active sites in most oxidation reactions, regulating their structure and distribution is crucial. However, manipulating the chemical environment of the Ov structure, such as by constructing surface region asymmetric Ov sites, has proven to be more critical.[10,11] Asymmetric Ov sites, with asymmetric coordination of Ov and cations, have advantages over their symmetric counterparts because of their unique metastable oxygen-binding features, which enable superior oxygen exchange capabilities.[10] Moreover, having an atomically dispersed metal stabilized on the surface of a substrate is an efficient strategy for creating asymmetric active sites, leading to the fabrication of highly efficient catalysts.[12,13] Conversely, water vapour is a ubiquitous component in most heterogeneous oxidation processes, such as water gas shift,[14] ozone decomposition,[15] and NO oxidation[16] reactions, and it is one of the final products of the oxidation of organic compounds. Several studies have revealed that water vapour strongly interacts with Ov sites, occupying active sites and hindering their reactions.[5,17,18] Isolated asymmetric Ov sites with robust redox capacity and exceptional water vapour resistance are essential for the efficient oxidation of organic compounds. However, the precise design and creation of atomic-level asymmetric Ov sites have rarely been explored. Anchoring isolated metal cations on a pristine metal oxide might be a straightforward and feasible approach for creating surface region asymmetric Ov sites.

Bismuth (Bi), a low-valence element (trivalent oxidation state), has been effectively utilized as a low-cost and high-performance component in environmental catalysis.[19] Moreover, Bi is frequently employed in aqueous phase oxidation reactions.[20,21] Owing to its combination of metallic and

[a]*State Key Laboratory for Ecological Security of Regions and Cities, Fujian Key Laboratory of Atmospheric Ozone Pollution Prevention, Xiamen Key Laboratory of Indoor Air and Health, Institute of Urban Environment, Chinese Academy of Sciences, Xiamen 361021, China. E-mail: huadeng@iue.ac.cn*

[b]*State Key Laboratory of Advanced Environmental Technology, Institute of Urban Environment, Chinese Academy of Sciences, Xiamen 361021, China*

[c]*University of Chinese Academy of Sciences, Beijing 100049, China*

[d]*School of Chemical Engineering, The University of Adelaide, North Terrace, Adelaide, SA 5005, Australia*

[e]*Research Centre for Eco-Environmental Sciences, Chinese Academy of Sciences, Beijing, 100085, China. E-mail: honghe@rcees.ac.cn*

[f]*Chair for Photonics and Optoelectronics, Department of Physics, Nano-Institute Munich, Ludwig-Maximilians-Universität München, Königinstr. 10, 80539 Munich, Germany*

[g]*Department of Earth and Environmental Science, Department of Chemistry, University of Pennsylvania, Philadelphia, PA 19104, USA. E-mail: frjoseph@sas.upenn.edu*

† These authors contributed equally to the work and are co-first authors.

nonmetallic properties, Bi doping might offset the humidity-related limitations of heterogeneous gas–solid processes. Nevertheless, ensuring the uniform dispersion rather than clustering of Bi cations on the surface of a support is crucial for their effectiveness.

Typically, the use of α-MnO_2 as a support for Bi using conventional approaches results in Bi atoms being anchored onto the outer surface of α-MnO_2 (Scheme 1a), resulting in a limited ability to tune Ov structures. As a pioneering strategy, we (Scheme 1b) introduce a nanocrystal-to-crystal transformation (CCT) approach for anchoring Bi atoms onto MnO_2. This catalyst, termed α-MnO_2–Bi and abbreviated as MnO_2–Bi, easily creates isolated asymmetric Bi–Ov–Mn sites. The structural properties of MnO_2–Bi are characterized using techniques such as extended X-ray absorption fine structure (EXAFS), positron annihilation lifetime spectroscopy (PALS), *in situ* Raman spectroscopy and density functional theory (DFT) calculations. Asymmetric Bi–Ov–Mn sharply reduces the competitive adsorption of water vapour and simultaneously maintains the ability of O_3 to activate the formation of reactive oxygen species (ROS) such as ˙OH. This material, assisted by ozone, can efficiently degrade various inert volatile organic compounds (VOCs) at ambient temperatures under realistic humid conditions. This work provides valuable insights into the development of functional asymmetric entities that integrate oxygen vacancies and single atoms for environmental catalysis and can guide the design of a catalyst for the removal of VOC under real and complex conditions.

Results and discussion

Textural and physicochemical properties of the catalysts

The synthesis of MnO_2–*x*Bi is based on a CCT approach, with the Bi loading controlled by varying the concentration of $Bi(NO_3)_3$. Inductively Coupled Plasma (ICP) analysis of the Bi contents in MnO_2–*x*Bi reveals that the measured values closely match the calculated theoretical weight fractions (Table S1). The XRD patterns in Fig. S1a show that MnO_2–1Bi, MnO_2–5Bi, and MnO_2–10Bi align closely with the standard α-MnO_2 structure (PDF #44-0141), indicating that Bi cations are uniformly distributed among Mn atoms without forming crystalline Bi oxides when the Bi loading level is below 10 wt%.[22] However, at 50 wt% Bi, either $Bi_2Mn_4O_{10}$ or Bi_2O_3 is detected in MnO_2–50Bi.[23] The broadening and slight redshift of the characteristic Raman peaks[24] of α-MnO_2 with increasing Bi content, as illustrated in Fig. S1b, suggest the formation of asymmetric Bi–O–Mn or Bi–Ov–Mn sites.

The morphologies of pristine MnO_2, MnO_2–*x*Bi and Bi/α-MnO_2 are illustrated in Fig. S2 and 1a–c. The pristine MnO_2 sample has a nanowire structure, while stacked nanorods emerge and increase with increasing Bi content. Compared with the clear and regular lattice fringes of the (2 0 0) surface plane of

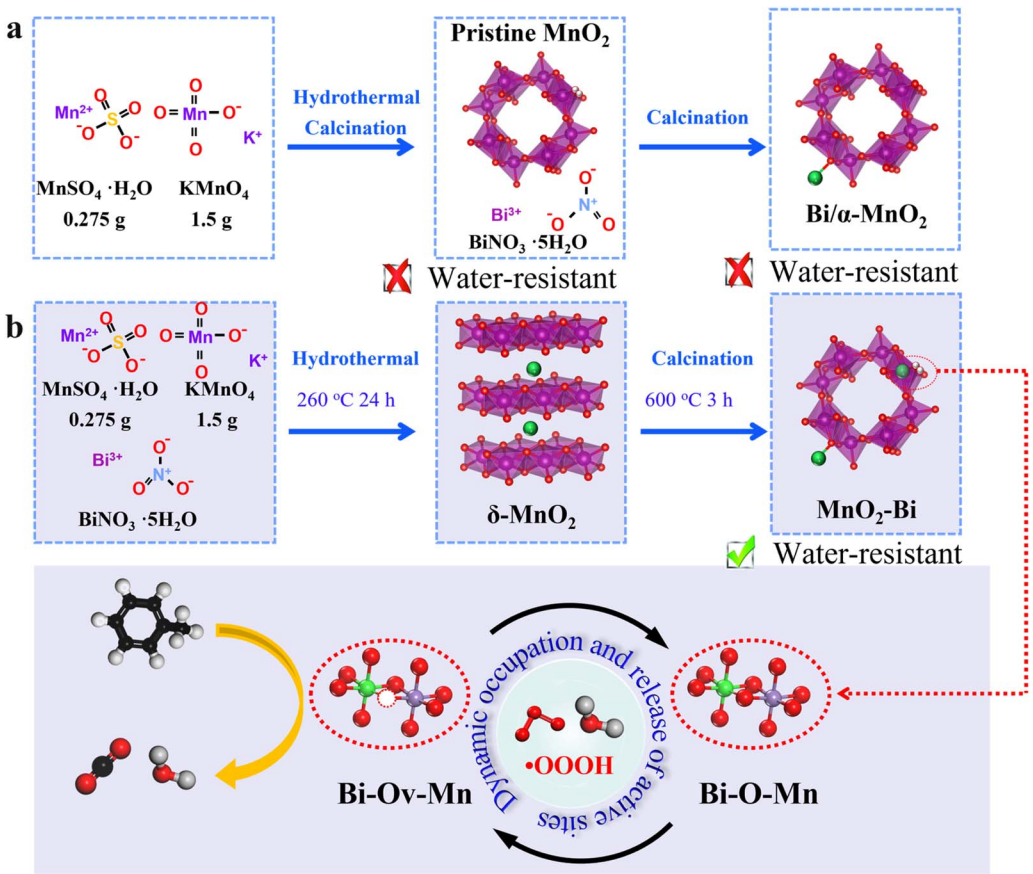

Scheme 1 Schematic diagram of catalyst preparation: (a) Bi/α-MnO_2 and (b) MnO_2–Bi.

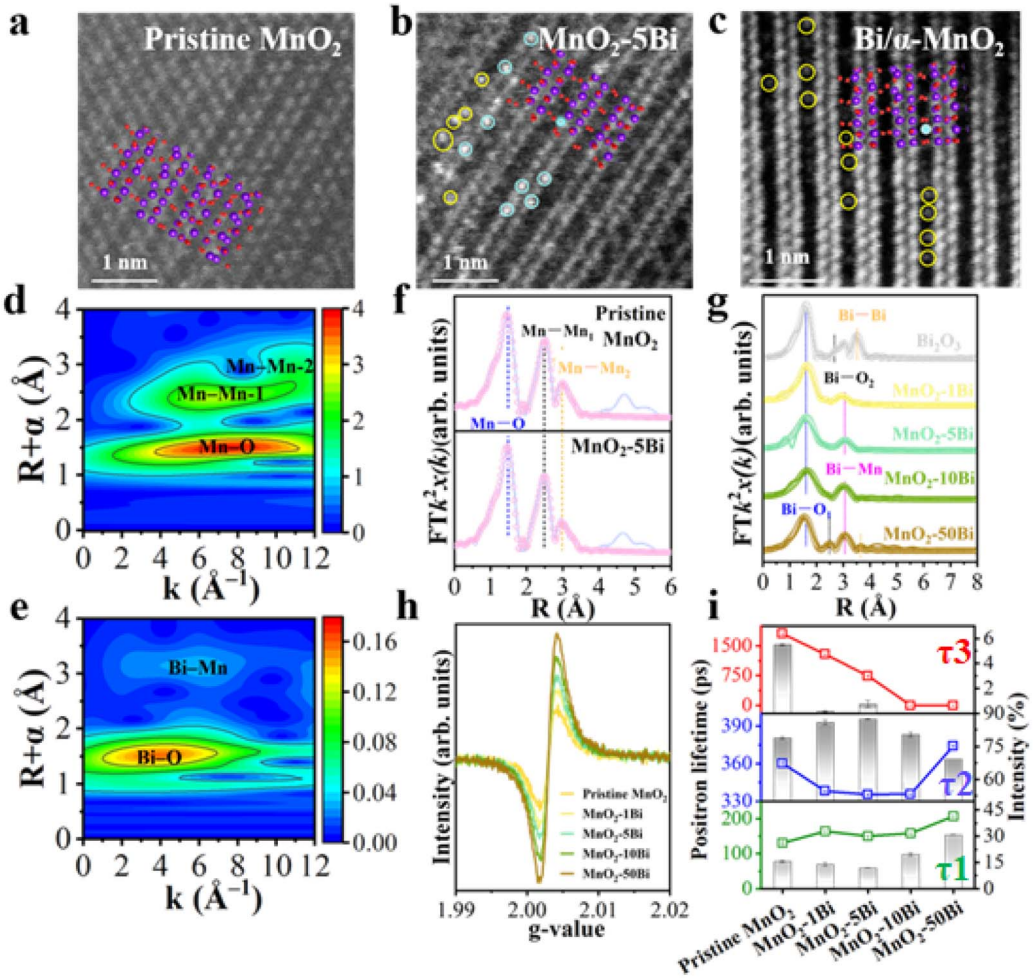

Fig. 1 Characterization results for the pristine MnO_2 and MnO_2–*x*Bi catalysts. (a–c) Representative aberration-corrected-STEM images of pristine MnO_2, MnO_2–5Bi and Bi/α-MnO_2 catalysts. (d and e) Wavelet transform images of the Mn K-edge and Bi K-edge for the MnO_2–5Bi catalysts. (f and g) EXAFS and corresponding fitted spectra of the Mn K-edge and Bi K-edge for pristine MnO_2 and MnO_2–*x*Bi catalysts. (h) ESR spectra. (i) Positron lifetimes and corresponding intensities.

MnO_2, some distorted lattice fringes are observed in MnO_2–*x*Bi, with (2 0 0) and (2 1 1) serving as the exposed planes. No discernible clusters are detected in the samples *via* high-angle annular dark-field scanning TEM (HAADF-STEM). STEM-coupled EDS elemental mapping, as depicted in Fig. S3, confirms the uniform distribution of Bi in MnO_2. Aberration-corrected transmission electron microscopy (STEM) images (Fig. 1a–c) reveal that in the MnO_2–5Bi catalyst, Bi is atomically dispersed both on the framework (yellow dots, empty tunnels) and lattice fringes (cyan dots) of α-MnO_2. Conversely, the Bi/α-MnO_2 sample shows Bi atoms dispersed on the framework but not within the lattice fringes. The pore structures and specific surface areas (SSAs) are determined by N_2 adsorption/desorption measurements (Fig. S4 and Table S1). The pore structures are basically maintained after various levels of Bi incorporation, although the SSA values decrease with increasing Bi loading.

XAFS results are obtained to analyse the local atomic structures and defect sites (Fig. 1d–g, S5 and Table S2). The curve-fitting results of the Mn K-edge EXAFS of MnO_2 (Fig. 1f and Table S2) reveal the presence of reduced Mn–O coordination numbers, suggesting the production of oxygen vacancies (Ovs) near the Mn sites. Fig. 1g and Table S2 show that the Bi–O coordination numbers increase with increasing Bi content. Bi anchoring results in the formation of a Mn–Bi shell, and the peak intensity increases with increasing Bi content. At low Bi-doping levels (<10 wt%), Bi atoms remain isolated and are separated by Mn, forming Bi–O–Mn. However, the Fourier transform peak of the MnO_2–50Bi sample suggests the coexistence of a Bi–Bi shell (Fig. S5b), indicating clustering at relatively high Bi loadings.

The chemical elements present and their electronic states in the MnO_2–Bi samples are investigated using X-ray photoelectron spectroscopy (XPS; Fig. S6), which reveals that the metal species are present only in oxidized states (Mn^{4+} at 643.5 eV, Mn^{3+} at 642.0 eV, and Bi^{3+} at 164.1 eV and 158.9 eV) rather than in metallic states.[25,26] The electron spin resonance (ESR) spectra in Fig. 1h indicate that the Ov signal at a *g* value of 2.003 increases with increasing Bi content, suggesting the creation of additional Ovs. The positron lifetimes (τ) and occupancies (*I*) shown in

Fig. 1i and Table S1 indicate that there are three distinct Ov environments:[27] isolated Ovs within the lattice (τ_1, 130.7–207.2 ps) and Ov clusters (τ_2, 335.4–374.3 ps), with τ_3 (743–1804 ps) representing positron lifetimes in the pore structure. The abundance of Ov clusters, as evidenced by the high I_2 value (69.2–87.4%), underscores their dominance among oxygen vacancies, a feature with reduced τ_2 values (from 360 to 335 ps) that is further amplified by appropriate Bi anchoring. This enhancement creates Bi–Ov–Mn sites with higher electron density compared to pristine MnO_2, highlighting the effective modulation of the electronic structure by Bi.

In short, the XRD, Raman and electron microscopy results suggest that at low levels of Bi anchoring, Bi cations are atomically distributed by substituting for Mn in the α-MnO_2 lattice, while excess Bi leads to the formation of Bi oxides. The ESR results reveal that the Ov content increases with increasing Bi content, and the PALS results further verify that the loading of isolated Bi atoms facilitates the formation of asymmetric Bi–Ov–Mn clusters.

Enhanced ozone activation and moisture resistance abilities due to Bi doping

Through ESR analysis, we detect ROS in the MnO_2 or MnO_2–xBi/ozone/water three-phase systems (Fig. 2a–d). An increased Bi content promotes $^1O_2$ and $^{\cdot}OH$ generation while reducing $^{\cdot}O_2^-$

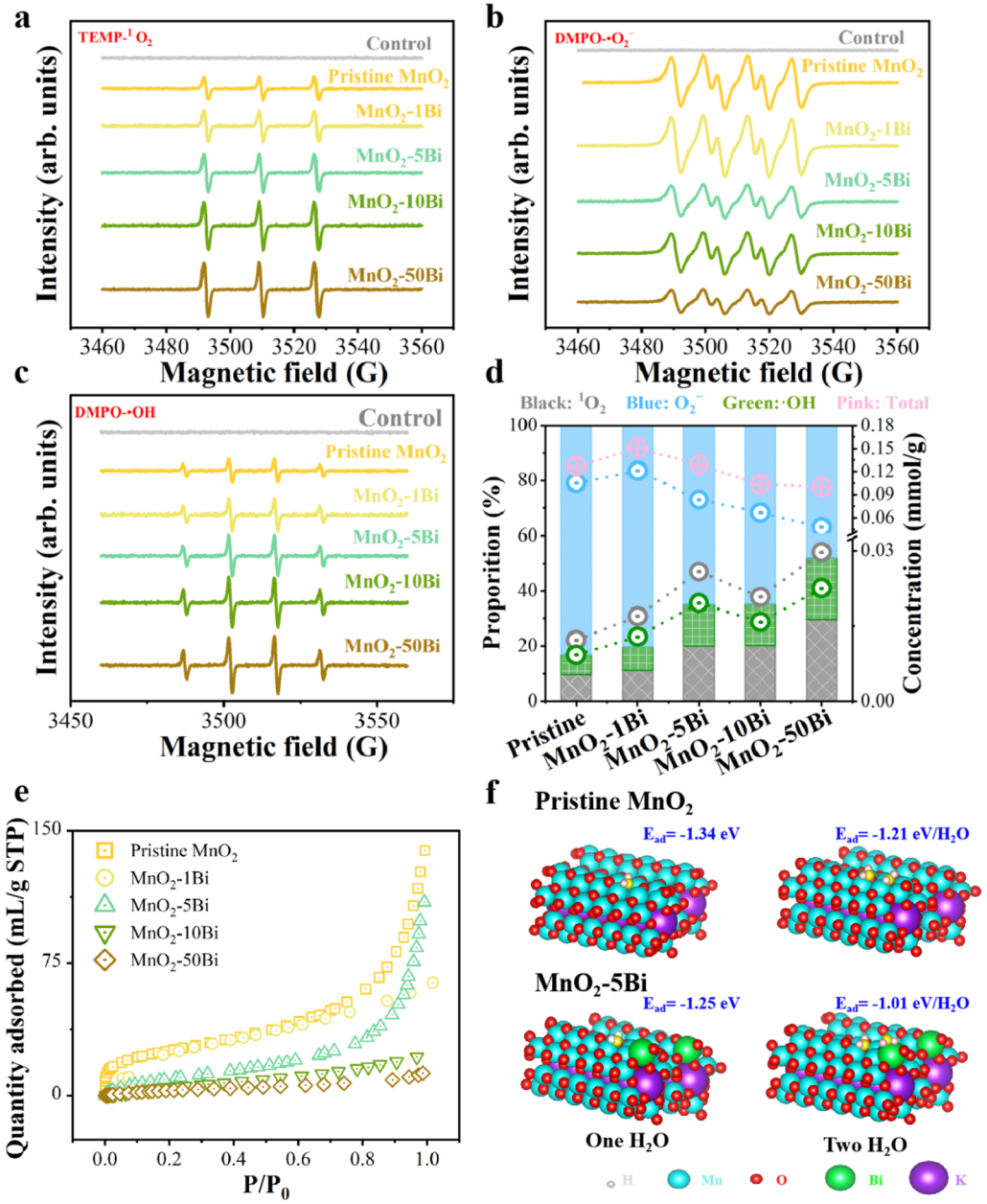

Fig. 2 Chemical properties of the pristine MnO_2 and MnO_2–xBi catalysts. (a–d) ESR spectra of the ROS when the pristine MnO_2 and MnO_2–xBi catalysts are exposed to O_3 in the dark. (e) Static adsorption isotherms for water. (f) Optimized adsorption structures for water on pristine MnO_2 and MnO_2–Bi with dimer vacancies.

formation. This result suggests that symmetric structures favour $^{\bullet}O_2^-$ production, whereas asymmetric structures are more effective for $^1O_2$ and $^{\bullet}OH$ production. DFT calculations are conducted to reveal the Ov structures and to propose an O_3 activation mechanism (see Text S3 for details). The optimized Ov structures are presented in Fig. S7. Compared with bare α-MnO_2, Bi loading decreases the energy required for Ov formation,[28] aligning with the ESR results shown in Fig. 1h. The variations in the adsorption energy and structure of O_3, including bond lengths and angles, are detailed in Fig. S8 and Table S3, respectively. Compared with a pristine Bi-anchored (2 0 0) slab, the Ov species increases O_3 activation, with substantial deformation of the O_3 molecule upon adsorption on the oxygen dimer vacancy cluster. This result is further confirmed by the evident electron transfer between the adsorbate and the asymmetric dimer Ov, as shown in Fig. S9. By combining these results with our previous findings,[28] we can deduce that oxygen dimer vacancies, whether symmetric or asymmetric, serve as efficient active sites for ozone activation.

Additionally, we investigate water vapour adsorption on pristine MnO_2 and MnO_2–Bi catalysts *via* static water vapour adsorption. Fig. 2e shows that the water adsorption amount decreases with increasing Bi loading, indicating that the asymmetric entities (Bi–Ov–Mn) significantly reduce water vapour adsorption. DFT calculations further verify the impact of asymmetric Bi–Ov–Mn sites on water vapour adsorption. As shown in Fig. 2f, Bi doping significantly reduces the water affinity at the vacancy sites due to the decreased adsorption energy, regardless of water coverage. This finding aligns with the static water adsorption results.

Interface evolution of asymmetric Bi–Ov–Mn linkages during ozonation

The structural changes in the catalysts and the dynamics of catalytic ozonation are analysed using *in situ* Raman spectroscopy, as depicted in Fig. S10 and 3a, b. Fig. 3a shows that MnO_2–5Bi has the highest peak intensities at 839 cm^{-1} (O_2^{2-}) and 1676 cm^{-1} (adsorbed O_3),[29–31] indicating that ozone activation is most effective with this catalyst. MnO_2–50Bi exhibits poor ozone activation due to its inadequate redox capability, as shown in Fig. S11. Under humid conditions (Fig. 3b), pristine MnO_2 produces fewer ROS as water occupies the active sites. In contrast, MnO_2–5Bi maintains peak intensity, indicating that the process of Bi anchoring increases ozone adsorption and activation, even in the presence of water.

Above, we confirm that the asymmetric oxygen vacancy structure formed by Bi addition effectively enhances O_3 activation and reduces water adsorption, thereby benefiting the catalytic ozonation of VOCs. To elucidate the benefits of asymmetric Bi–Ov–Mn in generating water resistance, DFT calculations are conducted to study the interactions between O_3 and

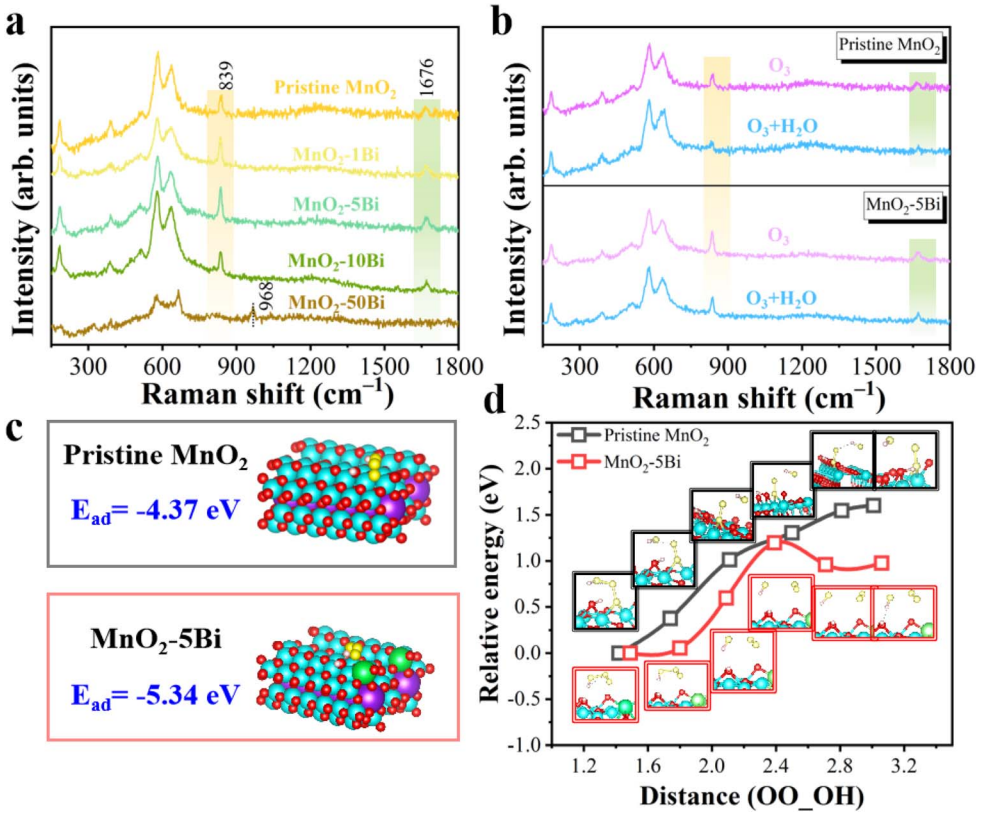

Fig. 3 *In situ* Raman spectra and DFT calculation results. (a) *In situ* Raman spectra of pristine MnO_2 and MnO_2–*x*Bi in ozone gas. (b) *In situ* Raman spectra of pristine MnO_2 and MnO_2–5Bi with the addition of water. (c) Theoretical models of $^{\bullet}OOOH$ on MnO_2 and MnO_2–5Bi catalysts. (d) Potential energy surface scanning for $^{\bullet}OOOH$ along the middle O–O bond.

H_2O molecules. The DFT results in Fig. 3c indicate that Bi anchoring reduces the formation energy of $^*OOOH$. A potential energy scan is performed for the $^*OOOH$ species along the linear axis of the middle O–O bond (Fig. 3d). Near Bi–Ov–Mn, the energetically favourable formation of active ROS occurs, thereby promoting $^*OH$ formation. Consequently, the asymmetric Bi–Ov–Mn moiety is expected to function as an active site because of its ability to activate both water and ozone.

To investigate the electronic mechanism, the electron transfer and density of states (DOS) associated with the activation of O_3 are analysed. Unlike O_3 in a vacuum layer, the O_3 molecules undergo dissociative adsorption on both pristine MnO_2 and MnO_2–Bi (Fig. S12), further verifying their ability to activate O_3. To better understand the nature of symmetric Mn–Ov–Mn and asymmetric Bi–Ov–Mn sites, the interactions of H_2O and O_3 with pristine MnO_2, MnO_2–Bi and Bi/α-MnO_2 (200) surfaces are investigated (Fig. 4 and S13). Unlike H_2O in a vacuum layer, H_2O molecules undergo similar dissociative adsorption on the surfaces of the pristine MnO_2, MnO_2–Bi and Bi/α-MnO_2 catalyst surfaces (Fig. S13). O_3 exhibits significantly different electron delivery (Bader charge) patterns across the above three surfaces in the presence of water vapour. For the pristine MnO_2 and Bi/α-MnO_2 catalysts, which feature symmetric Mn–Ov–Mn entities, the electron accumulation in both terminal oxygen atoms of adsorbed O_3 is identical, as shown in Fig. 4b and d, indicating symmetric electronic redistribution. In contrast, the electronic transfer to the terminal oxygen atoms of O_3 on asymmetric Bi–Ov–Mn (MnO_2–Bi catalyst) is asymmetric. Owing to the unique metal and nonmetal characteristics of Bi, the electron donation to the nearest terminal oxygen atom is less than that to the other terminal oxygen atoms (+0.24 *vs.* +0.59*e*), as illustrated in Fig. 4c. Moreover, the DOS pattern of MnO_2–Bi exhibits a significantly greater density of unpaired electron spins than those of the MnO_2 and Bi/α-MnO_2 catalysts. This observation aligns with the experimental results (Fig. 2d), which show that the asymmetric Bi–Ov–Mn structure promotes the generation of ROS.

Subsequent investigations aim to thoroughly explore the catalytic ozonation activity and reaction mechanism of pristine MnO_2 and MnO_2–Bi catalysts to verify the impact of asymmetric Ov units on VOC ozonation under humid conditions.

Catalytic ozonation performance

The CCT method outperforms traditional preparation methods in controlling the generation of Ovs in MnO_2 (Fig. S14 and S15). Thus, the catalytic activity under various conditions is examined carefully. While pristine MnO_2 synthesized using the CCT strategy exhibits superior catalytic activity under dry conditions, its performance significantly decreases under humid conditions (Fig. S16). This limitation is effectively mitigated by the incorporation of foreign atoms. The introduction of promoters such as Co, La and particularly Bi into the MnO_2 lattice markedly enhances both toluene conversion and CO_2 yield in the presence of water vapour (Fig. S17), confirming the general applicability of the CCT strategy for doping various metals. Furthermore, by optimizing the Bi concentration, we further improve catalytic ozonation, achieving superior performance under humid conditions (Fig. 5b and S18). MnO_2–5Bi presents the highest CO_2 yield of 0.65 μmol g^{-1} s^{-1} at less than 0.5 vol%

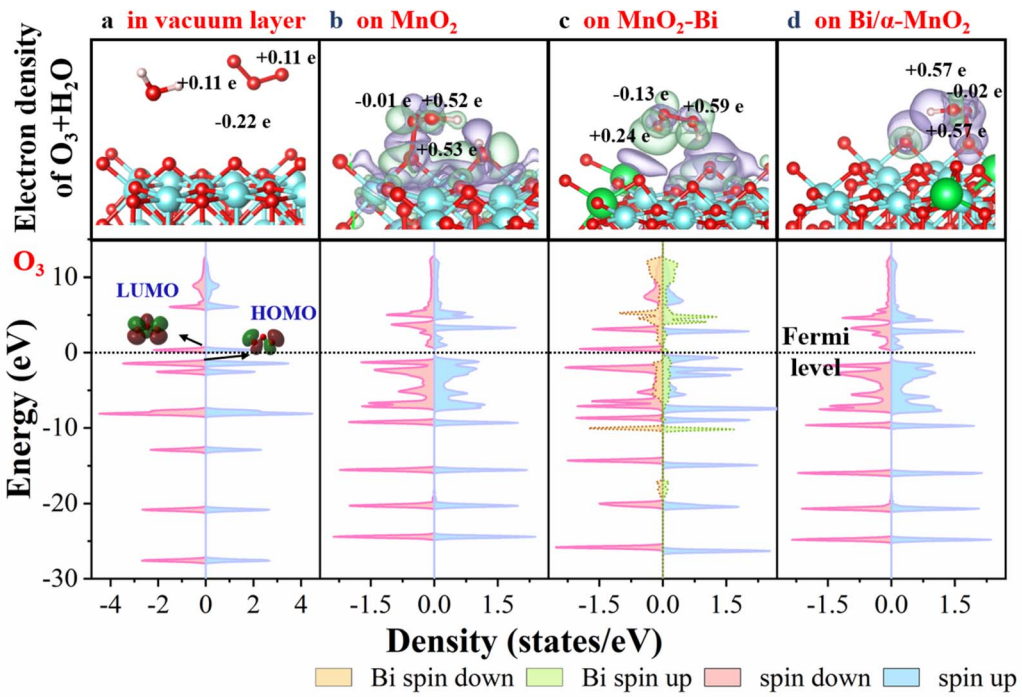

Fig. 4 Electron density difference and DOS analysis of O_3 for O_3 + H_2O in the vacuum layer (a), on MnO_2 (b), on MnO_2–Bi (c), and on Bi/α-MnO_2 (d). The cyan and green colours indicate a decrease and increase in the electron density, respectively.

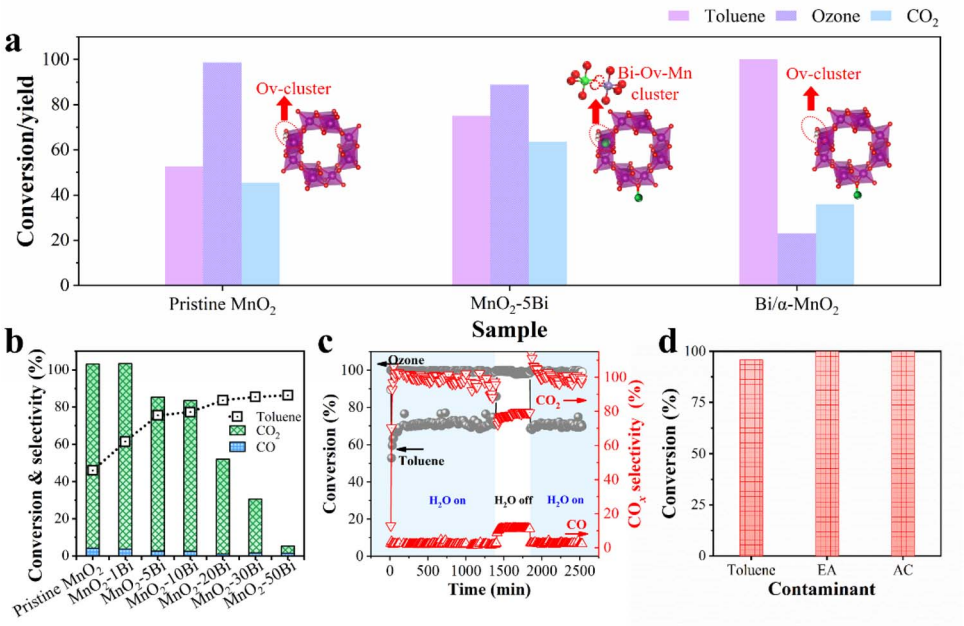

Fig. 5 Catalytic ozonation performance. (a) Catalytic ozonation of toluene over various catalysts under humid conditions at 190 min (toluene: 100 ppm, ozone: 1600 ppm, 120 L h^{-1} g^{-1}, reaction temperature: 30 °C, water: 1.1 vol%). (b) Catalytic ozonation efficiency of toluene over MnO_2–*x*Bi catalysts at 300 min (toluene: 100 ppm, ozone: 1400 ppm, WHSV: 120 L h^{-1} g^{-1}, reaction temperature: 30 °C, water: 1.1 vol%). (c) Long-term activity of MnO_2–5Bi for the catalytic ozonation of toluene (toluene: 100 ppm, ozone: 2000 ppm, WHSV: 60 L h^{-1} g^{-1}, reaction temperature: 30 °C, water: 1.8 vol%; if used, RH = 42%). (d) Catalytic ozonation of mixed VOCs (33.3 ppm AC + 33.3 ppm EA + 33.3 ppm toluene, ozone: 1600 ppm, WHSV: 120 L h^{-1} g^{-1}, reaction temperature: 30 °C, water: 0.6 vol%).

moisture. In contrast to MnO_2–5Bi, Bi/α-MnO_2 with the same Bi loading level is produced by doping Bi onto the outer surface of MnO_2 following the same CCT approach. The catalytic performance is shown in Fig. 5a. As expected, the Bi/α-MnO_2 catalyst exhibits notably inferior catalytic activity compared with that of MnO_2–5Bi. The substitution of Bi for Mn within the α-MnO_2 lattice particularly facilitates the formation of asymmetric Bi–Ov–Mn structures. In contrast, the interaction between Bi and the outer surface of MnO_2 is too weak to form the single-site Bi–Ov–Mn entity; instead, it leads to the formation of Mn–Ov–Mn entities, as illustrated in Fig. 1b, c and 4c, d. In summary, this phenomenon underscores the efficacy of the single-site Bi–Ov–Mn entity resulting from the substitution of lattice Mn with Bi.

The effects of differences in weight hourly space velocity (WHSV), reaction temperature and initial ozone concentration on catalyst performance are presented in Fig. S19. The stability test of the MnO_2–5Bi catalyst with 1.8 vol% water vapour reveals that it maintains stable toluene conversion and high CO_2 selectivity (Fig. 5c and S20). Fig. 5d and S21 confirm the efficiency of MnO_2–5Bi in degrading various VOCs, including acetone (AC), ethyl acetate (EA), toluene and their mixture. Table S4 summarizes the catalytic ozonation performance of various catalysts from recent studies, highlighting the outstanding activity and stability of our catalysts in VOC elimination. It should be noted, however, that real waste gas streams contain complex components such as dust and acid gases. Therefore, investigating the catalyst's performance under actual industrial conditions represents a critical next step.

Taking toluene as an example, the catalytic oxidation mechanism is revealed by GC-MS analysis (Fig. S22). The intermediates are summarized in Table S5. The pristine MnO_2 catalyst primarily produces benzaldehyde, acetophenone, and benzoic acid, while MnO_2–5Bi generates acetic acid. Under humid conditions, pristine MnO_2 exhibits a reduced peak intensity of the byproduct, which is correlated with decreased activity because water accumulation blocks the active sites. Conversely, the main byproduct of MnO_2–5Bi shifts to amylene, and its activity remains stable, demonstrating its superior moisture resistance. Collectively, the identified intermediates outline a comprehensive degradation network wherein toxic aromatics are sequentially broken down into low-carbon acids and finally mineralized to CO_2 and H_2O, confirming the efficacy and environmental benefit of the process.

Conclusion

We synthesized a series of MnO_2–*x*Bi catalysts *via* the CCT synthetic method, adjusting the Bi content to tune the lattice oxygen environment, resulting in the formation of an asymmetric Bi–O–Mn moiety. These units, particularly the MnO_2–5Bi variant, demonstrated exceptional redox behaviour and water resistance due to the metastable nature of the oxygen sites, increasing ozone activation even in the presence of water. DFT calculations confirmed that water molecules interacted more actively and released ˙OH more readily from these sites, particularly at oxygen vacancy dimers. Thus, the superior catalytic performance of MnO_2–5Bi was due partially to the dynamic occupation and exposure of active sites—specifically, the asymmetric Bi–Ov–Mn dimer—by water molecules. To our knowledge, this work is the first report on the fabrication of

water-resistant Mn-based catalysts using the simple CCT synthetic method. The current strategy has far-reaching implications for designing and preparing numerous water-resistant metal oxidation catalysts and can serve as a potential forefront in VOC degradation technology, especially with regard to its use in practical applications.

Author contributions

Yuqin Lu designed and performed the experiments, analyzed the data and wrote the original draft of the paper. Huayang Zhang analyzed the data and contributed to modify the manuscript. Jianguo Ding and Tingting Pan performed the experiments. Wenjie Tian, Yunbo Yu, Changbin Zhang, Wenpo Shan and Shaobin Wang analyzed the data. Hua Deng conducted the theoretical calculations. Hua Deng, Hong He and Joseph S. Francisco supervised the project and contributed to modify the manuscript. All authors contributed to the preparation of the manuscript.

Conflicts of interest

The authors declare no competing financial interests.

Data availability

The data that support the findings of this study are available upon reasonable request from the corresponding author.

Supplementary information: catalyst preparation and activity, catalyst characterization and DFT calculations. See DOI: **https://doi.org/10.1039/d5sc06166k**.

Acknowledgements

This work was funded by the National Natural Science Foundation of China (52270111, 52570134, 52500128, 52225004), Fujian Provincial Natural Science Foundation of China (2024J010042) and the Foundation of Institute of Urban Environment, the guiding project of seizing the commanding heights of "self-purifying city" (No. IUE-CERAE-202401). W. T. acknowledges the partial support from the Australian Research Council Discovery Early Career Researcher Award (ARC DECRA) (Project ID: DE220101074), and H. Z. and S. W. acknowledge the support from the Australian Research Council Discovery Project (DP230102406).

References

1 R. Yang, Y. Fan, R. Ye, Y. Tang, X. Cao, Z. Yin and Z. Zeng, MnO_2-Based materials for environmental applications, *Adv. Mater.*, 2021, **33**, e2004862.

2 H. Yan, B. Liu, X. Zhou, F. Meng, M. Zhao, Y. Pan, J. Li, Y. Wu, H. Zhao, Y. Liu, X. Chen, L. Li, X. Feng, D. Chen, H. Shan, C. Yang and N. Yan, Enhancing polyol/sugar cascade oxidation to formic acid with defect rich MnO_2 catalysts, *Nat. Commun.*, 2023, **14**, 4509.

3 C. T. Campbell and C. H. F. Peden, Oxygen vacancies and catalysis on ceria surfaces, *Science*, 2005, **309**, 713–714.

4 S. Polarz, J. Strunk, V. Ischenko, M. W. E. van den Berg, O. Hinrichsen, M. Muhler and M. Driess, On the role of oxygen defects in the catalytic performance of zinc oxide, *Angew. Chem., Int. Ed.*, 2006, **45**, 2965–2969.

5 R. Schaub, P. Thostrup, N. Lopez, E. Lægsgaard, I. Stensgaard, J. K. Nørskov and F. Besenbacher, Oxygen vacancies as active sites for water dissociation on rutile TiO_2(110), *Phys. Rev. Lett.*, 2001, **87**, 266104.

6 R. Zhang, L. Pan, B. Guo, Z.-F. Huang, Z. Chen, L. Wang, X. Zhang, Z. Guo, W. Xu, K. P. Loh and J.-J. Zou, Tracking the role of defect types in Co_3O_4 structural evolution and active motifs during oxygen evolution reaction, *J. Am. Chem. Soc.*, 2023, **145**, 2271–2281.

7 G. Zhuang, Y. Chen, Z. Zhuang, Y. Yu and J. Yu, Oxygen vacancies in metal oxides: recent progress towards advanced catalyst design, *Sci. China Mater.*, 2020, **63**, 2089–2118.

8 M. V. Ganduglia-Pirovano, A. Hofmann and J. Sauer, Oxygen vacancies in transition metal and rare earth oxides: Current state of understanding and remaining challenges, *Surf. Sci. Rep.*, 2007, **62**, 219–270.

9 Y. Zheng, K. Fu, Z. Yu, Y. Su, R. Han and Q. Liu, Oxygen vacancies in a catalyst for VOCs oxidation: synthesis, characterization, and catalytic effects, *J. Mater. Chem. A*, 2022, **10**, 14171–14186.

10 K. Yu, L. L. Lou, S. Liu and W. Zhou, Asymmetric oxygen vacancies: the intrinsic redox active sites in metal oxide catalysts, *Adv. Sci.*, 2020, **7**, 1901970.

11 S. Zhao, D. Kang, Y. Liu, Y. Wen, X. Xie, H. Yi and X. Tang, Spontaneous formation of asymmetric oxygen vacancies in transition-metal-doped CeO_2 nanorods with improved activity for carbonyl sulfide hydrolysis, *ACS Catal.*, 2020, **10**, 11739–11750.

12 L. Nie, D. Mei, H. Xiong, B. Peng, Z. Ren, X. I. P. Hernandez, A. DeLaRiva, M. Wang, M. H. Engelhard, L. Kovarik, A. K. Datye and Y. Wang, Activation of surface lattice oxygen in single-atom Pt/CeO_2 for low-temperature CO oxidation, *Science*, 2017, **358**, 1419–1423.

13 T. Li, F. Liu, Y. Tang, L. Li, S. Miao, Y. Su, J. Zhang, J. Huang, H. Sun, M. Haruta, A. Wang, B. Qiao, J. Li and T. Zhang, Maximizing the number of interfacial sites in single-atom catalysts for the highly selective, solvent-free oxidation of primary alcohols, *Angew. Chem., Int. Ed.*, 2018, **57**, 7795–7799.

14 A. Chen, X. Yu, Y. Zhou, S. Miao, Y. Li, S. Kuld, J. Sehested, J. Liu, T. Aoki, S. Hong, M. F. Camellone, S. Fabris, J. Ning, C. Jin, C. Yang, A. Nefedov, C. Wöll, Y. Wang and W. Shen, Structure of the catalytically active copper–ceria interfacial perimeter, *Nat. Catal.*, 2019, **2**, 334–341.

15 C. Chen, J. Xie, X. Chen, W. Zhang, J. Chen and A. Jia, Cu species-modified OMS-2 materials for enhancing ozone catalytic decomposition under humid conditions, *ACS Omega*, 2023, **8**, 19632–19644.

16 L. Chen, D. Ren, X. Hou, J. Zhang, Y. Wu, Y. Wang, C. Hu, P. Duan, C. Li, C.-Y. Chiang, C. He and Q. Lu, Asymmetric

oxygen vacancy-enriched Mn_2O_3@CeO_2 for NO oxidation with excellent low-temperature activity and boosted SO_2-resistance, *Appl. Catal., B*, 2024, **340**, 123202.

17 R. S.-d.-A. Jaime Oviedo, M. Á. S. Miguel and J. F. Sanz, Methanol and water dissociation on TiO_2 (110): The role of surface oxygen, *J. Phys. Chem. C*, 2008, **112**, 17737–17740.

18 Y. Du, N. A. Deskins, Z. Zhang, Z. Dohnálek, M. Dupuis and I. Lyubinetsky, Two pathways for water interaction with oxygen adatoms onTiO_2 (110), *Phys. Rev. Lett.*, 2009, **102**, 096102.

19 Z. Ni, Y. Sun, Y. Zhang and F. Dong, Fabrication, modification and application of $(BiO)_2CO_3$-based photocatalysts: A review, *Appl. Surf. Sci.*, 2016, **365**, 314–335.

20 Y. Qiu, J. Zhou, J. Cai, W. Xu, Z. You and C. Yin, Highly efficient microwave catalytic oxidation degradation of p-nitrophenol over microwave catalyst of pristine α-Bi_2O_3, *Chem. Eng. J.*, 2016, **306**, 667–675.

21 P. Li, R. Miao, P. Wang, F. Sun and X. Li, Bi-metal oxide-modified flat-sheet ceramic membranes for catalytic ozonation of organic pollutants in wastewater treatment, *Chem. Eng. J.*, 2021, **426**, 131263.

22 T. Gao, H. Fjellvåg and P. Norby, A comparison study on raman scattering properties of α- and β-MnO_2, *Anal. Chim. Acta*, 2009, **648**, 235–239.

23 C. Díaz-Guerra, P. Almodóvar, M. Camacho-López, S. Camacho-López and J. Piqueras, Formation of β-Bi_2O_3 and δ-Bi_2O_3 during laser irradiation of Bi films studied in-situ by spatially resolved raman spectroscopy, *J. Alloys Compd.*, 2017, **723**, 520–526.

24 E. Hastuti, A. Subhan, P. Amonpattaratkit, M. Zainuri and S. Suasmoro, The effects of Fe-doping on MnO_2: phase transitions, defect structures and its influence on electrical properties, *RSC Adv.*, 2021, **11**, 7808–7823.

25 Q. Lian, L. Hu, D. Ma, Y. Jiao, D. Xia, Y. Huang, Z. Tang, W. Qu, H. Zhao, C. He and D. D. Gang, Interstitial atomic Bi charge-alternating processor boosts twofold molecular oxygen activation enabling rapid catalytic oxidation reactions at room temperature, *Adv. Funct. Mater.*, 2022, **32**, 2205054.

26 G. Zhu, W. Zhu, Y. Lou, J. Ma, W. Yao, R. Zong and Y. Zhu, Encapsulate alpha-MnO_2 nanofiber within graphene layer to tune surface electronic structure for efficient ozone decomposition, *Nat. Commun.*, 2021, **12**, 4152.

27 D. J. Keeble, J. Wiktor, S. K. Pathak, L. J. Phillips, M. Dickmann, K. Durose, H. J. Snaith and W. Egger, Identification of lead vacancy defects in lead halide perovskites, *Nat. Commun.*, 2021, **12**, 5566.

28 Y. Lu, H. Deng, T. Pan, C. Zhang and H. He, Thermal annealing induced surface oxygen vacancy clusters in α-MnO_2 nanowires for catalytic ozonation of VOCs at ambient temperature, *ACS Appl. Mater. Interfaces*, 2023, **15**, 9362–9372.

29 C. Reed, Y. Xi and S. Oyama, Distinguishing between reaction intermediates and spectators: a kinetic study of acetone oxidation using ozone on a silica-supported manganese oxide catalyst, *J. Catal.*, 2005, **235**, 378–392.

30 Y. Huang, D. Ma, W. Liu, D. Xia, L. Hu, J. Yang, P. Liao and C. He, Enhanced catalytic ozonation for eliminating CH_3SH via graphene-supported positively charged atomic Pt undergoing Pt^{2+}/Pt^{4+} redox cycle, *Environ. Sci. Technol.*, 2021, **55**, 16723–16734.

31 W. Li, G. V. Gibbs and S. T. Oyama, Mechanism of ozone decomposition on a manganese oxide catalyst. 1. In situ raman spectroscopy and Ab initio molecular orbital calculations, *J. Am. Chem. Soc.*, 1998, **120**, 9041–9046.